Phase transitions in thermoelectric Mg-Ag-Sb thin films

Nouredine Oueldna, Alain Portavoce, Maxime Bertoglio, Andréa Campos, Abelkhalek Kammouni, Khalid Hoummada

To cite this version:

Nouredine Oueldna, Alain Portavoce, Maxime Bertoglio, Andréa Campos, Abelkhalek Kammouni, et al.. Phase transitions in thermoelectric Mg-Ag-Sb thin films. Journal of Alloys and Compounds, 2021, 900, 10.1016/j.jallcom.2021.163534 . hal-04040829

HAL Id: hal-04040829

https://hal.science/hal-04040829v1

Submitted on 22 Mar 2023

Journal of Alloys and Compounds 900 (2022) 163534

Contents lists available at ScienceDirect

Journal of Alloys and Compounds

journal homepage: www.elsevier.com/locate/jalcom

Phase transitions in thermoelectric Mg-Ag-Sb thin films

Nouredine Oueldna[a,b], Alain Portavoce[a,*], Maxime Bertoglio[a], Andréa Campos[c], Abelkhalek Kammouni[b], Khalid Hoummada[a]

[a] *Aix-Marseille University - CNRS, IM2NP Faculté des Sciences de Saint-Jérôme case 142, 13397 Marseille, France*
[b] *LASMAR, University of Moulay Ismail, Faculté des Sciences 11 201, Meknes, Morocco*
[c] *Aix Marseille University, CNRS, Centrale Marseille, FSCM (FR1739), CP2M, F-13397 Marseille, France*

ARTICLE INFO

Article history:
Received 30 September 2021
Received in revised form 20 December 2021
Accepted 28 December 2021
Available online 30 December 2021

Keywords:
MgAgSb
Phase transitions
In-situ X-ray diffraction
Thin films
Thermoelectricity

ABSTRACT

α-MgAgSb thin films are expected to be compatible with the complementary metal oxide semiconductor (CMOS) technology, and could be used to develop thermoelectric modules integrated to microelectronic devices for energy harvesting. However, bulk studies showed that the presence of secondary phases in addition to α-MgAgSb, such as the metallic phase Ag_3Sb, deteriorates the thermoelectric properties. Consequently, understanding phase transformations in Mg-Ag-Sb thin films produced by CMOS-compatible magnetron sputtering is capital for the production of homogeneous α-MgAgSb thin films to be used in energy harvesting thermoelectric modules integrated into microelectronic devices. In this work, different Mg-Ag-Sb films were deposited by magnetron sputtering using either a single alloyed target with the average composition $Mg_{1/3}Ag_{1/3}Sb_{1/3}$ or using Mg, Ag, Sb co-deposition from three elementary targets. In situ X-ray diffraction measurements were used to investigate the phase transitions in the films, aiming to determine the thermal stability of α-MgAgSb and to investigate the possibility of producing α-MgAgSb films without secondary phases. The results show that the use of the single alloyed target does not allow the production of homogenous α-MgAgSb films. The phase formation sequence observed in the films is different from bulk samples in this case. Co-sputtering of the three elements Mg, Ag, and Sb, allowing the composition of the as-deposited film to be better controlled, confirmed that the $Mg_{1/3}Ag_{1/3}Sb_{1/3}$ stoichiometry does not allow the production of homogenous α-MgAgSb films. Contrasting with usual belief, the results show that the Ag and Sb compositions of the phases α-MgAgSb and γ-MgAgSb vary during annealing, and the phase transitions α-to-β, β-to-γ, and α-to-γ are not allotropic. These finding are of major importance for the production of the thermoelectric compound α-MgAgSb, and explain the large variations of the α-MgAgSb Seebeck coefficient reported in the literature.

1. Introduction

The increase of functionality of mobile technologies has led to an increase of energy consumption, limiting the autonomy of mobile devices. In this context, new technologies allowing for environmental energy harvesting (EH) are currently investigated [1–5]. These energy-harvesting devices should enable the autonomy of mobile devices to be extended by either partially recharging the battery of the device or allowing some operations to be performed without using the energy stored in the battery.

In the case of technologies such as micro-sensors, microelectronics integrated circuits (IC) etc., for which part of the energy is thermally lost, the integration of thermoelectric devices appears as a potential EH solution [6–11]. For this purpose, the integrated thermoelectric device should be based on nanostructures, such as thin films, elaborated with industrial processes compatible with the complementary metal oxide semiconductor (CMOS) technology [12–15], and the material application domain should be around room temperature. Bismuth telluride based compounds are known as the best materials operating at room temperature and have attracted a wide attention [16–18]. However, these materials are toxic and scarce [19,20] as well as not CMOS-compatible. Hence, the development of alternative CMOS-compatible high-efficient thermoelectric materials made from non-toxic and earth-abundant elements is crucial.

Tremendous research studies on bulk MgAgSb-based materials have been conducted since 2012. MgAgSb was first described as a promising *p*-type thermoelectric material by Kirkham et al. and Zhao

---

[*] Corresponding author.
E-mail address: alain.portavoce@im2np.fr (A. Portavoce).

https://doi.org/10.1016/j.jallcom.2021.163534

et al. [21,22]. They studied the different crystal structures of MgAgSb and reported a high thermoelectric figure of merit $ZT \sim 1$ at room temperature (RT) for the phase α-MgAgSb, which can be increased by doping [22–29]. Compared to the traditional Bi_2Te_3 based solid solutions, the elements in the composition of α-MgAgSb are in extremely high abundance and have a low toxicity.

Bulk MgAgSb presents three different crystal structures as a function of temperature: the phase α at RT, the phase β at intermediate temperatures, and the phase γ at high temperatures [30]. α-MgAgSb has a tetragonal structure corresponding to the space group ($I\bar{4}c2$). The RT lattice parameters are $a = 9.1631$ Å and $c = 12.701$ Å [31]. The Ag site-filling pattern for this phase forms one-dimensional chains of unfilled Mg-Sb pseudo-cubes in all three primary directions. The resulting unit cell is a superlattice with three different types of Ag atoms (Ag^1, Ag^2 and Ag^3) depending on their position. β-MgAgSb also crystallizes in a tetragonal structure corresponding to the space group (P4/nmm). It is stable between 588 and 633 K. The structure is similar to the Cu_2Sb structure with Mg and Ag atoms occupying one of the two Cu sites. γ-MgAgSb is a half-Heusler with a cubic structure corresponding to the space group ($F\bar{4}3m$). It is stable at temperatures higher than 633 K, but was also observed at RT after cooling [21]. Among these three phases, only α-MgAgSb presents interesting thermoelectric properties close to RT. However, achieving the fabrication of a homogeneous α phase remains a serious challenge, while its thermoelectric properties are considerably influenced by the presence of undesired phases such as Ag_3Sb [21–24,32–37]. Indeed, contrasting with other alloys [38], Mg-Ag-Sb secondary phases are detrimental to α-MgAgSb thermoelectric properties. For example, a bulk α-MgAgSb matrix containing the secondary phases Ag_3Sb and Sb shows a reduced $ZT \sim 0.5$ [21]. The difficulty of obtaining a homogeneous α phase is generally attributed to a very small equilibrium window (temperature and composition) of this ternary phase. However, no data are currently available regarding the ternary phase diagram of Mg-Ag-Sb at low temperatures. Frost [39] gives the Mg-Ag-Sb ternary phase diagram only at 450 °C and 550 °C, and the stability limits of the phase α-MgAgSb at these temperatures are not in agreement with experimental data reported at RT [23].

To date, MgAgSb has been only studied in its bulk state using elaboration methods incompatible with the CMOS technology. However, α-MgAgSb thin films produced by CMOS-compatible magnetron sputtering may be used for the integration of EH devices in microelectronics technology [6,40–42]. Furthermore, α-MgAgSb nanocrystalline thin films may present improved thermoelectric properties due to nano-effects such as a higher Seebeck coefficients (charge carrier energy filtering [43–45]) or a lower thermal conductivity [28]. Thus, it is important to study the stability of α-MgAgSb in thin films as well as their properties for thermoelectric applications.

This work reports the fabrication of 300 nm-thick Mg-Ag-Sb films by magnetron sputtering using two different methods (alloyed target or co-sputtering), as well as the study of Mg-Ag-Sb phase stability up to 823 K in the thin films using in situ X-ray diffraction (XRD). Despite the significant control offered by the magnetron sputtering technique on the amount of deposited materials (controlled thickness below 3 nm), elaboration of homogeneous α-MgAgSb films is not trivial. The results show that the phase transitions α-to-β, β-to-γ, and α-to-γ are not allotropic, and that the phases α-MgAgSb and γ-MgAgSb are not stoichiometric compounds.

2. Experiments

300 nm-thick Mg-Ag-Sb films were deposited on the silicon native oxide of commercial Si(001) wafers using a commercial magnetron sputtering setup exhibiting a base pressure of 10^{-8} Torr. The thin SiO_2 layer was used as a diffusion barrier, preventing any interactions between the film and Si. All the samples were deposited at RT using the same 99.9999% pure argon gas flow (3.10^{-3} mbar). The samples were rotating at a rate of 5 rpm during deposition in order to improve thickness homogeneity.

Two different deposition conditions were used: for the first set of samples (#1), the Mg-Ag-Sb film was obtained from the 150 W DC sputtering of a single 99.99% pure Mg-Ag-Sb alloyed target exhibiting the averaged Mg:Ag:Sb stoichiometry 1/3:1/3:1/3 purchased from CODEX international. The Mg-Ag-Sb film growth rate was 1.41 nm s^{-1}. For the second set of samples (#2), the Mg-Ag-Sb film was obtained from the co-sputtering of three 99.999% pure Ag, Mg and Sb elementary targets supplied by CODEX international. The Mg and Sb targets were sputtered in the DC mode, while the Ag target was sputtered in the RF mode. The deposition flux of each target was calibrated thanks to the measurement by X-ray reflectivity of the thickness of pure Mg, Ag, or Sb films deposited at RT on the native SiO_2 layer of Si(001) substrates, considering a sticking coefficient of unity. The sputtering power of the Mg and Sb targets was set to 133 W, while the sputtering power of the Ag target was set to 150 W, corresponding to the stoichiometry $Mg_{1/3}Ag_{1/3}Sb_{1/3}$ and to a global growth rate of 5.17 nm s^{-1}. The composition of the as-deposited films was determined using Energy Dispersive X-ray Spectroscopy (EDS) measurements, performed with an EDAX Octane Silicon Drift Detector (129 eV energy resolution for Manganese) on a Zeiss Gemini 500 field emission gun scanning electron microscope (SEM) operating at 10 kV. In situ XRD measurements were performed in the Bragg-Brentano geometry (θ-2θ), using a Cu Kα source ($\lambda_{K\alpha}$= 0.154 nm). The samples were loaded in an Anton Paar TTK 600 chamber under vacuum (10^{-6} Torr) equipped with a heating stage, in a Philips X′pert MPD system equipped with an X′celerator PSD detector designed for high-speed data collection. The temperature (T) was increased from 303 to 823 K using 5 K min^{-1} steps and five minute-long XRD acquisitions, which correspond to an average temperature ramp of 0.5 K min^{-1}. The phase identification was performed using the X′Pert High Score software package for diffraction data analysis (files #96-154-3082 for α-MgAgSb, #96-154-3081 for β-MgAgSb, #96-154-3080 for γ-MgAgSb, #96-101-1093 for Ag_3Sb, and #00-035-0732 for Sb).

3. Results and discussion

3.1. Phase transitions in thin films sputtered from the $Mg_{1/3}Ag_{1/3}Sb_{1/3}$ alloyed target

Fig. 1a shows the diffractograms acquired during in situ annealing of samples #1. The XRD intensity is presented as color gradients (from blue to red for low to high intensity) versus the Bragg-Brentano angle 2θ (20–65°) on the abscissa axis and the annealing temperature on the ordinate axis. The as-deposited film already presents five diffraction peaks at RT at $2\theta = 34.42°$, 37.21°, 39.39°, 51.72°, and 61.77°, respectively corresponding to the atomic planes (101), (020), (111), (022), and (103) of the same binary phase Ag_3Sb (Fig. 1). The XRD peaks correspond to Ag_3Sb nano-grains distributed in an amorphous matrix [41]. The intensity of these diffraction peaks increases during annealing due to the growth of the Ag_3Sb nano-grains, and at $T \sim 433$ K eleven additional diffraction peaks appear simultaneously (Fig. 1b). Eight diffraction peaks at $2\theta = 24.2°$, 26.14°, 31.68°, 41.12°, 44.75°, 53.37°, 58.1°, and 59.39° respectively belong to the atomic planes (202), (220), (114), (411), (422), (433), (008), and (514) of the phase α-MgAgSb; and three peaks at $2\theta = 28.88°$, 40.18°, and 42.12° respectively belong to the atomic planes (012), (104), and (110) of the Sb crystal. The diffraction peaks of the phase α-MgAgSb disappear at $T \sim 713$ K, concomitantly with the appearance of six peaks at $2\theta = 23.09°$, 38.01°, 44.93°, 54.85°, 60.25°, and 61.03° respectively corresponding to the atomic planes (111), (022), (222), (040), (133), and (042) of the phase γ-MgAgSb (Fig. 1a). The phase transitions observed during the annealing ramp correspond to the

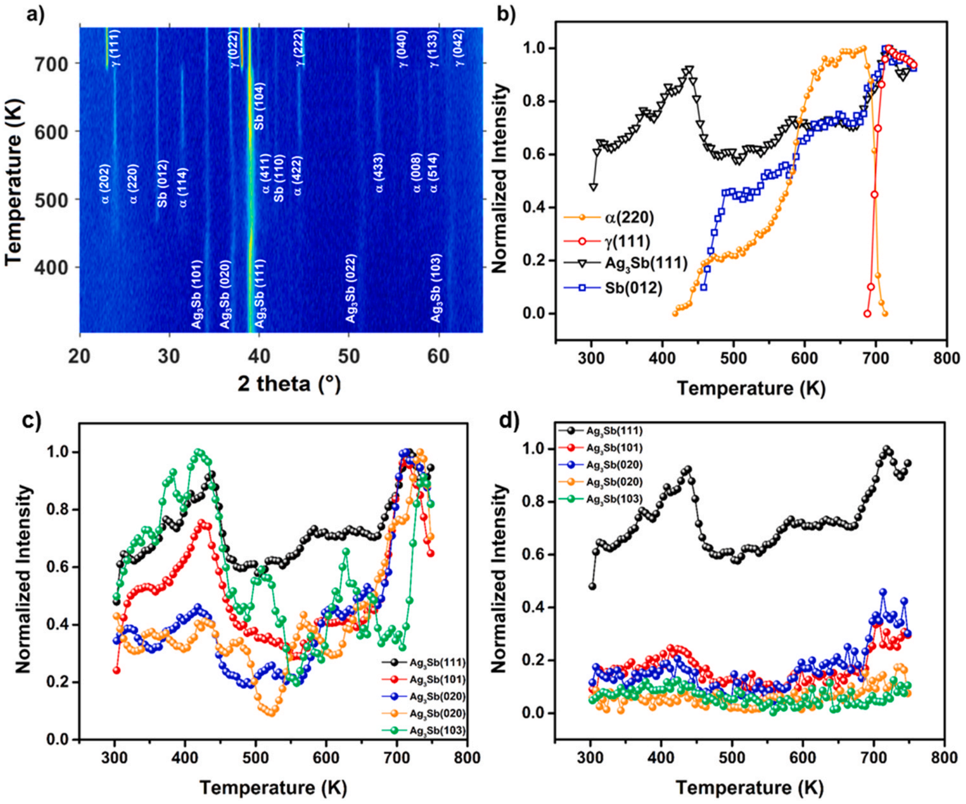

Fig. 1. a) X-ray diffractograms (20° ≤ 2θ ≤ 60°) acquired at different temperatures during in situ ramp annealing of samples #1 from 303 to 753 K; variations of integrated and normalized XRD peak intensities versus temperature measured during the same annealing: b) α-MgAgSb(220) (spheres), γ-MgAgSb(111) (open circles), Ag_3Sb(101) (open triangles) and Sb(012) (open squares); c) Ag_3Sb detected peak variations versus temperature normalized to their maximum; and d) Ag_3Sb detected peak variations versus temperature normalized to the maximum of the peak Ag_3Sb(111).

three steps: (RT) $Ag_3Sb \rightarrow$ (433 K) $Ag_3Sb + Sb + \alpha \rightarrow$ (713 K) $Ag_3Sb + Sb + \gamma$. According to bulk observations [21], α-MgAgSb is expected to transform into β-MgAgSb at T ~ 588 K, and β-MgAgSb is expected to transform into γ-MgAgSb at T ~ 633 K. β-MgAgSb is not observed in the present case, and the stability domain of α-MgAgSb is extended from 588 K to 713 K (ΔT = 125 K). But as observed in bulk, the phase α coexists with the two undesired phases Ag_3Sb and Sb. Fig. 1b shows the variations of the integrated diffraction peak intensities of each phase during the ramp annealing. The figure presents only the variations of the highest intensity peak of each phase. Indeed, during growth or consumption, the intensities of all the diffraction peaks of a same phase vary simultaneously in the same way and at the same rate. The presented measurements being normalized, the addition of the contribution of all the peaks gives the same results as that obtained from the diffraction peak with the highest intensity. As an example, Fig. 1c presents the integrated intensity variations of all the diffraction peaks of Ag_3Sb normalized to their maximum during the ramp annealing. All the peak intensity variations are similar, only the peaks (020) and (103) present some fluctuations. Fig. 1d presents the same intensity variations normalized to the maximum intensity of the peak (111) that shows the highest diffraction intensity. It shows that the (020) and (103) peak fluctuations are actually due to detection limit, as the peaks (020) and (103) present the lowest intensities. Furthermore, considering the contribution of other peaks than that of the peak (111) does not significantly change the results. Fig. 1b shows that part of Ag_3Sb is consumed during the formation of the phase α, while Ag and Sb are rejected during the α-to-γ transition, as the diffracted intensity (i.e. the volume) of Ag_3Sb and Sb increases with the increase of the diffracted intensity of the phase γ. These observations lead to the conclusion that: i) the film stoichiometry does not correspond to the stoichiometry of the phase α in the investigated temperature range (above 433 K), the film contains an excess of Ag and Sb compared to Mg (no Mg phase observed); and ii) the phases α and γ do not possess the same stoichiometry, α is richer in both Ag and Sb.

Fig. 2a presents in situ XRD measurements acquired during the sample cooling under vacuum (heater switched off). The phase transition observed during cooling corresponds to the two steps: (823 K) $Ag_3Sb + Sb + \gamma \rightarrow$ (513 K) $Ag_3Sb + Sb + \gamma + \alpha$, which is identical to the observations made in bulk [21]. Atom transport is progressively reduced during cooling, and only allotropic phase transitions are generally observed. The phase α appears at T = 513 K during cooling and its diffraction intensity increase is proportional to the diffraction intensity decrease of the phase γ (Fig. 2b). However, only a small fraction of γ is changed to α, and the main fraction of γ is still observed back to RT. This is in agreement with a different stoichiometry between the phases α and γ, as in this case atomic transport is needed for the transformation, and is prevented due to the temperature decrease below 513 K. Indeed, Sb diffracted intensity is constant during cooling (Fig. 2b). However, the diffracted intensity of Ag_3Sb increases during cooling from T ~ 650 K down to T ~ 450 K (Fig. 2b). The reason for this behavior is not obvious, but the increase of Ag_3Sb XRD intensity appears to be independent of the simultaneous growth of α and respectively consumption of γ, as it starts at a temperature more than one hundred of Kelvin higher than the γ-to-α transition. One can note that the α-to-γ transition occurs at T = 693 K during heating, while the γ-to-α transition occurs at T = 513 K during cooling, corresponding to a ΔT ~ 200 K. The α-to-γ transition is not observed in bulk as the phase β is detected before the phase γ. Nevertheless, the γ-to-α transition temperature in the thin film is close to that in bulk (T ~ 473 K). The shift of the γ-MgAgSb(111) peak observed versus temperature in Fig. 2a is mainly related to thermal expansion. Fig. 3 presents the coefficient of thermal expansion $\alpha_d = \Delta T \times d/\Delta d$ determined from the variations of the distance d

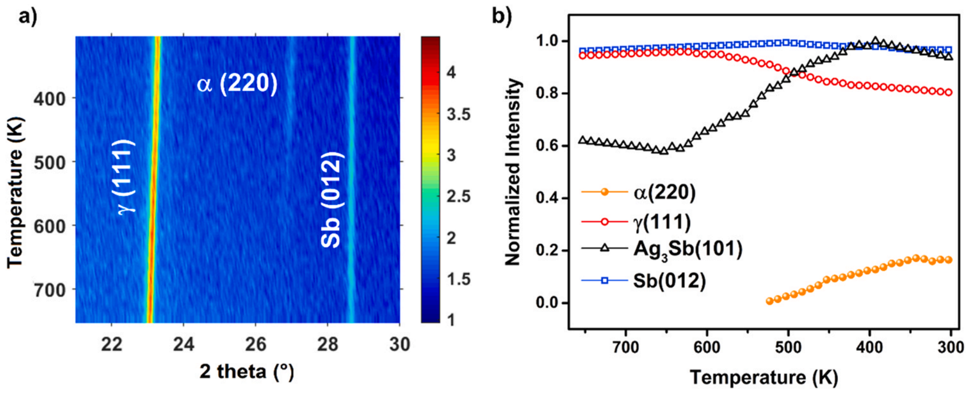

Fig. 2. a) X-ray diffractograms (20° ≤ 2θ ≤ 60°) acquired at different temperatures during in situ thermal cooling of samples #1 from 753 to 303 K, b) Variations of integrated and normalized XRD peak intensities versus temperature measured during the cooling: α-MgAgSb(220) (spheres), γ-MgAgSb(111) (open circles), $Ag_3Sb(101)$ (open triangles) and Sb (012) (open squares).

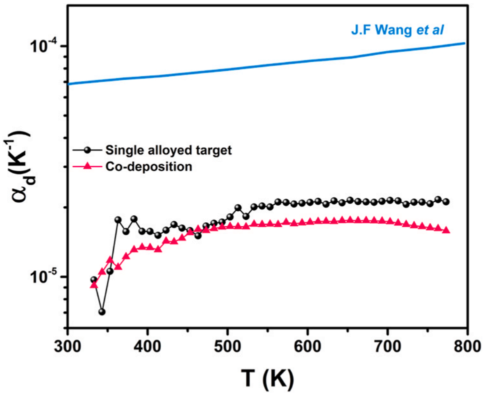

Fig. 3. Coefficient of thermal expansion α_d of γ-MgAgSb determined from de variations of the interatomic distance of γ-MgAgSb(111) planes during cooling. The experimental data are compared with calculations from Ref. [46].

between the planes (111) of γ-MgAgSb recorded during cooling. It is compared to the coefficient of thermal expansion calculated by Wang et al. [46]. The coefficient calculated by Wang et al. is in average about four times larger than the coefficient determined experimentally. Considering that thermal expansion may not be isotropic, our data corresponding to (111) planes nevertheless suggest that the shift of the γ-MgAgSb(111) diffraction peak is mainly related to thermal expansion.

Phase stability in relaxed bulk at given temperature depends on composition. However, phase stability can be more complex in thin films, as it includes surface and interface energy minimization effects, as well as stress effects due to the difference of volume and/or thermal expansion between the coexistent phases. Furthermore, phase nucleation in thin films is influenced by surface and interfaces (surface segregation and hetero-nucleation). Even so, missing the phase β-MgAgSb in the phase formation sequence during heating suggests that the film composition is different from the $Mg_{1/3}Ag_{1/3}Sb_{1/3}$ stoichiometry. The composition of the as-deposited film was found to be 27 at% of Mg, 38 at% of Ag, and 35 at% of Sb using EDS measurements. This composition is different from the stoichiometry $Mg_{1/3}Ag_{1/3}Sb_{1/3}$, but is still not too far off considering the usual EDS 2–3 at% error [47]. The overall composition of the sputtered target corresponds to $Mg_{1/3}Ag_{1/3}Sb_{1/3}$. However, the target is crystallized, and thus, contains different phases with probably an inhomogeneous distribution. Consequently, the sputtering rates of the elements Mg, Ag and Sb from the different phases in this target can be different and are not controlled. For example, the melting temperature of Mg (923 K) and Sb (904 K) being similar, their sputtering rates are expected to be comparable. However, their sputtering rate is expected to be significantly different from that of Ag, as the melting temperature of Ag (1235 K) is much higher. Thus, similar experiments are reported in the next section performed on samples #2. In this case, the Mg-Ag-Sb film exhibits the same thickness and was deposited using sputtering powers adjusted for each of the three elementary targets in order to independently control the elementary fluxes of Mg, Ag, and Sb. As expected, flux calibrations showed that the same sputtering power is used in order to get same Mg or Sb deposition fluxes, but a different sputtering power is needed for Ag. This way, the stoichiometry of samples #2 is expected to be $Mg_{1/3}Ag_{1/3}Sb_{1/3}$ with an error below 1%.

3.2. Phase transitions in thin films sputtered from Mg, Ag, and Sb elementary targets

Fig. 4 shows the diffractograms recorded versus temperature during the ramp annealing of samples #2. Similar to samples #1, five diffraction peaks are detected at RT after deposition at $2\theta = 34.42°$, 37.21°, 39.39°, 51.72°, and 61.77°, corresponding to the atomic planes (101), (020), (111), (022), and (103) of the binary phase Ag_3Sb. Thirteen additional peaks appear simultaneously at $T = 423$ K. Ten peaks at $2\theta = 23.95°$, 31.02°, 39.6°, 41.14°, 41.87°, 46.44°, 46.92°, 56.6°, 57.58°, and 58.8° respectively correspond to the atomic planes (202), (114), (224), (411), (330), (422), (206), (440), (008) and (514) of the phase α-MgAgSb, and three peaks at $2\theta = 23.53°$, 28.72°, and 48.21°, respectively correspond to the Sb atomic planes (003), (012), and (006). The XRD peaks of the phases Ag_3Sb and α vanish at $T = 623$ K while nine additional peaks appear concomitantly at 2θ = 23.97°, 31.45°, 38.97°, 40.85°, 43.02°, 44.55°, 53.29°, 57.97° and 59.08°, respectively corresponding to the atomic planes (101), (111), (112), (200), (201), (103), (004), (203), and (220) of the phase β-MgAgSb (Figs. 4 and 5). At the same time, Sb XRD intensity is constant (Fig. 5). Finally, at $T = 673$ K the β XRD peaks disappear concurrently with the appearance of two peaks at $2\theta = 23.07°$ and $2\theta = 47.07°$, corresponding to γ-MgAgSb(111) and γ-MgAgSb(222), respectively. Furthermore, the diffracted intensities of the phases Ag_3Sb and Sb increase during the growth of the phase γ up to 720 K (Fig. 5). At higher temperature, the diffracted intensities of Sb and of the phase γ are almost constant, while the diffracted intensity of Ag_3Sb decreases up to 823 K. In summary, the phase transitions observed during the annealing ramp correspond to the four steps: (RT) Ag_3Sb → (423 K) Ag_3Sb + Sb + α → (623 K) Sb + β → (673 K) Sb + Ag_3Sb + γ. β-MgAgSb is now observed in the phase sequence. The phase transitions versus temperature are in better agreement with the transitions reported in the case of bulk material suggesting that the overall composition of the film is closer to that of the experiments reported on bulk material. The composition of the as-deposited film was found to be 33 at% of Mg, 30 at% of Ag, and 37 at% of Sb using EDS

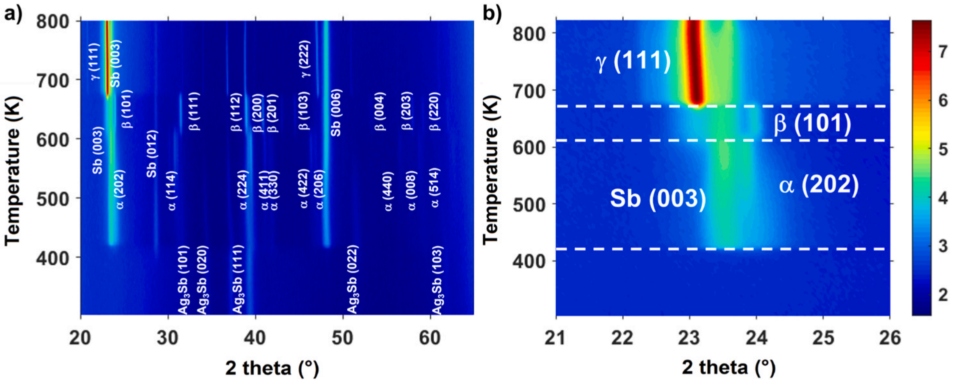

Fig. 4. a) X-ray diffractograms (20° ≤ 2θ ≤ 60°) acquired at different temperatures during in situ ramp annealing of samples #2 from 303 to 823 K, b) the same X-ray diffractograms for 21° ≤ 2θ ≤ 26°.

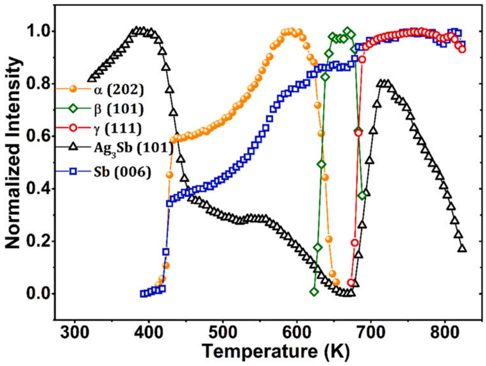

Fig. 5. Variations of integrated and normalized XRD peak intensities versus temperature measured during in situ ramp annealing of samples #2 from 303 to 823 K: α-MgAgSb(220) (spheres), β-MgAgSb(101) (open diamonds), γ-MgAgSb(111) (open circles), Ag_3Sb(101) (open triangles) and Sb(006) (open squares).

measurements, which is close to the stoichiometry $Mg_{1/3}Ag_{1/3}Sb_{1/3}$ considering EDS measurement error. However, three differences can be mentioned compared to bulk samples: i) the RT initial state of the as-deposited film before the formation of the phase α corresponds to an amorphous film containing Ag_3Sb nanocrystals, while the bulk samples already contained the three phases Ag_3Sb, Sb, and α-MgAgSb at RT after elaboration; ii) Ag_3Sb vanishes during the β-to-γ transition in thin films, while it is always present during annealing of bulk samples; and iii) the α-to-β and β-to-γ transitions occur at higher temperatures in thin films: $\Delta T = 623 - 588 = 35$ K for α-to-β and $\Delta T = 673–633 = 40$ K for β-to-γ.

Integration of the diffraction peak intensities (Fig. 5) shows that part of Ag_3Sb is consumed during the formation of the phases Sb and α, as observed during annealing of samples #1. Furthermore, Ag_3Sb is fully consumed during the α-to-β transition, while the Sb volume slightly increases, meaning that the phase β incorporated the Ag atoms contained in the Ag_3Sb phase, but not all the Sb coming from the same phase. However, Ag_3Sb reappears and the Sb volume again increases during the β-to-γ transition, meaning that Ag and Sb are rejected from the phase γ. The consumption of the phase Ag_3Sb observed for $T > 720$ K while the volumes of Sb and γ-MgAgSb are almost constant was also observed during the annealing of samples #1 (Fig. 1b). In the two cases (samples #1 and #2), the DRX intensity decrease is observed on all the detected peaks of Ag_3Sb, and thus, cannot be explained by Ag_3Sb grain growth competition. However, Ag_3Sb consumption could be related to an increase of Ag "solubility" in the phase γ with temperature. These observations lead to the conclusion that: i) the stoichiometry of the films #2 correspond to the stoichiometry $Mg_{1/3}Ag_{1/3}Sb_{1/3}$, but this stoichiometry may not correspond to the phase α in the investigated temperature range (above 433 K); ii) the phases α and β do not possess the same stoichiometry, β is significantly richer in Ag and richer in Sb; and iii) the phases β and γ do not possess the same stoichiometry, β is also significantly richer in Ag and Sb than γ, but the stoichiometry of γ may largely depends on temperature, the concentration of Ag and probably Sb increasing with temperature.

Fig. 6 presents in situ XRD measurements acquired during the sample cooling under vacuum. The phase transition observed during cooling corresponds to the two steps: (823 K) $Ag_3Sb + Sb + \gamma \rightarrow$ (473 K) $Ag_3Sb + Sb + \gamma + \alpha$. It is identical to the observations made on

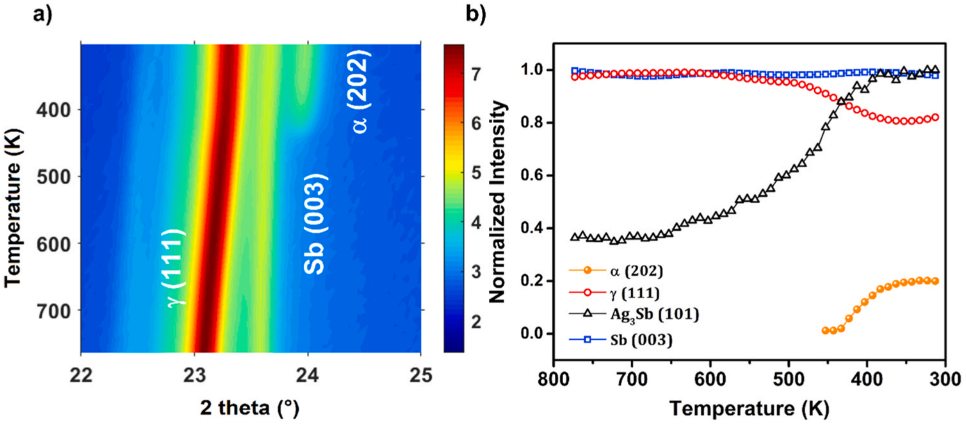

Fig. 6. a) X-ray diffractograms (20° ≤ 2θ ≤ 60°) acquired at different temperatures during in situ cooling of samples #2 from 773 to 313 K, b) Variations of integrated and normalized XRD peak intensities versus temperature measured during the cooling: α-MgAgSb(202) (spheres), γ-MgAgSb(111) (open circles), Ag_3Sb(101) (open triangles) and Sb (003) (open squares).

the samples #1 as well as in bulk [21]. However, the phase α appears at $T = 473$ K instead of 513 K for samples #1, which is the same temperature as in bulk. Similar to samples #1, the XRD intensity increase of the phase α is proportional to the XRD intensity decrease of the phase γ (Fig. 6b), and only a small fraction of γ is changed to α, the main fraction of γ being observed at RT. As mentioned before, the stability of γ during cooling could be explained by the difference of stoichiometry between the three phases γ, β, and α, and the atom mobility reduction due to cooling. Similar to the case of samples #1, the volume of the phase Sb is constant during cooling, while the volume of Ag_3Sb increases and reaches a plateau as well as γ and α at $T \sim 400$ K, as atomic transport is probably stopped below this temperature. Fig. 3 shows that α_d determined from samples #2 cooling is similar to that determined from samples #1.

4. Conclusion

Phase transitions in 300 nm-thick $Mg_{1/3}Ag_{1/3}Sb_{1/3}$ thin films deposited by magnetron sputtering have been studied using in situ XRD during an average temperature ramp of 0.5 K min^{-1}. Two types of samples were studied: samples #1 were deposited from a single alloyed target, while samples #2 were deposited from three elementary Mg, Ag, and Sb targets. The use of a single $Mg_{1/3}Ag_{1/3}Sb_{1/3}$ target (samples #1) does not allow a film with the initial target composition to be deposited, probably due to the difference of sputtering rate of the three elements Mg, Ag and Sb in the different phases present in the target. In this case, the phase β-MgAgSb is missing in the phase formation sequence compared to results obtained in bulk. Co-sputtering of three elementary Mg, Ag, and Sb targets (samples #2) allows the composition of the deposited films to be controlled. The binary phase Ag_3Sb is present in the as-deposited film, as in the reported case of bulk $Mg_{1/3}Ag_{1/3}Sb_{1/3}$ samples, and the phase formation sequence is the same as in bulk materials, excepted that the transition temperatures of the α-to-β and β-to-γ transformations are shifted to higher temperatures ($35 \leq \Delta T \leq 40$ K).

The comparison of the XRD intensity of the phases during the ramp annealing of the two samples leads to the conclusion that the phase transitions α-to-β, β-to-γ, and α-to-γ are not allotropic. The phases α, β and γ do not possess the same composition, and α and γ are not stoichiometric compounds. α is richer than γ in both Ag and Sb, and β is significantly richer in Ag and Sb than both α and γ, the composition of α and γ being closer than that of β. These results show that the thermoelectric phase α-MgAgSb should be obtained using a stoichiometry different from 1/3:1/3:1/3, which can vary with temperature. Furthermore, the phase α-MgAgSb accepting significant stoichiometry variations, significant variations of its Seebeck coefficient can be expected depending on elaboration conditions, in agreement with the variations already reported in the literature (74–240 µV K^{-1}).

CRediT authorship contribution statement

Nouredine Oueldna: Investigation, Writing – original draft, Visualization. **Alain Portavoce:** Conceptualization, Validation, Writing – original draft, Supervision, Project administration. **Maxime Bertoglio:** Validation, Resources. **Andréa Campos:** Investigation. **Abelkhalek Kammouni:** Validation, Supervision, Funding acquisition. **Khalid Hoummada:** Conceptualization, Writing – review & editing, Project administration, Funding acquisition.

Declaration of Competing Interest

The authors declare that they have no known competing financial interests or personal relationships that could have appeared to influence the work reported in this paper.

Acknowledgement

The authors would like to thank Prof. Dr. Dominique Mangelinck for XRD analysis software.

This work was financially supported by CAMPUS FRANCE-PHC TOUBKAL 2018 (French-Morocco bilateral program) Grant number: TBK/18/65.

References

[1] T.M. Tritt, Thermoelectric phenomena, materials, and applications, Annu. Rev. Mater. Res. 41 (2011) 433–448, https://doi.org/10.1146/annurev-matsci-062910-100453
[2] E. Flage-Larsen, O.Martin Lovvik, Thermoelectrics and its Energy Harvesting: Materials, Preparation, and Characterization in thermoelectrics, (2016), https://doi.org/10.1109/NCM.2008.43
[3] W. Liu, Y. Lan, J. Sui, Z. Liu, Z. Ren, Materials for near-room temperatures, Advanced Thermoelectrics, CRC Press, Taylor & Francis Group, Boca Raton, FL, 2018, pp. 67–106, https://doi.org/10.1201/9781315153766-3
[4] G. Tan, L.D. Zhao, M.G. Kanatzidis, Rationally designing high-performance bulk thermoelectric materials, Chem. Rev. 116 (2016) 12123–12149, https://doi.org/10.1021/acs.chemrev.6b00255
[5] S. Twaha, J. Zhu, Y. Yan, B. Li, A comprehensive review of thermoelectric technology: materials, applications, modelling and performance improvement, Renew. Sustain. Energy Rev. 65 (2016) 698–726, https://doi.org/10.1016/j.rser.2016.07.034
[6] A.P. Perez-Marín, A.F. Lopeandía, L. Abad, P. Ferrando-Villaba, G. Garcia, A.M. Lopez, F.X. Muñoz-Pascual, J. Rodríguez-Viejo, Micropower thermoelectric generator from thin Si membranes, Nano Energy 4 (2014) 73–80, https://doi.org/10.1016/j.nanoen.2013.12.007
[7] S.B.K. Moorthy, Thin Film Structures in Energy Applications, Oxford University Press, 2015, https://doi.org/10.1007/978-3-319-14774-1
[8] D.D. Pineda, A. Rezania, Thermoelectric Energy Conversion: Basic Concepts and Device Applications, Wiley, 2017.
[9] L.E. Bell, Cooling, heating, generating power, and recovering waste heat with thermoelectric systems, Science 321 (2008) 1457–1461, https://doi.org/10.1126/science.1158899
[10] G. Li, H. Ahmoum, S. Liu, S. Liu, M.S. Su'ait, M. Boughrara, M. Kerouad, Q. Wang, Theoretical insight into magnetic and thermoelectric properties of Au doped ZnO compounds using density functional theory, Phys. B Condens. Matter 562 (2019) 67–74, https://doi.org/10.1016/j.physb.2019.03.020
[11] H. Ahmoum, G. Li, S. Belakry, M. Boughrara, M.S. Su'ait, M. Kerouad, Q. Wang, Structural, morphological and transport properties of Ni doped ZnO thin films deposited by thermal co-evaporation method, Mater. Sci. Semicond. Process. 123 (2021) 105530, https://doi.org/10.1016/j.mssp.2020.105530
[12] J.P. Gambino, E.G. Colgan, Silicides and ohmic contacts, Mater. Chem. Phys. 52 (1998) 99–146, https://doi.org/10.1016/S0254-0584(98)80014-X
[13] H. Park, D. Lee, G. Park, S. Park, S. Khan, J. Kim, W. Kim, Energy harvesting using thermoelectricity for IoT (internet of things) and E-skin sensors, J. Phys. Energy 1 (2019) 42001, https://doi.org/10.1088/2515-7655/ab2f1e
[14] R. Feng, F. Tang, N. Zhang, X. Wang, Flexible, High-power density, wearable thermoelectric nanogenerator and self-powered temperature sensor, ACS Appl. Mater. Interfaces 11 (2019) 38616–38624, https://doi.org/10.1021/acsami.9b11435
[15] C.S. Kim, H.M. Yang, J. Lee, G.S. Lee, H. Choi, Y.J. Kim, S.H. Lim, S.H. Cho, B.J. Cho, Self-powered wearable electrocardiography using a wearable thermoelectric power generator, ACS Energy Lett. 3 (2018) 501–507, https://doi.org/10.1021/acsenergylett.7b01237
[16] G.J. Snyder, E.S. Toberer, Complex thermoelectric materials, Nat. Mater. 7 (2008) 105–114, https://doi.org/10.1038/nmat2090
[17] J.P. Heremans, V. Jovovic, E.S. Toberer, A. Saramat, K. Kurosaki, A. Charoenphakdee, S. Yamanaka, G.J. Snyder, Enhancement of thermoelectric efficiency in PbTe by distortion of the electronic density of states, Science 321 (2008) 554–557, https://doi.org/10.1126/science.1159725
[18] D.A. Wright, Thermoelectric properties of bismuth telluride and its alloys, Nature 181 (1958) 834, https://doi.org/10.1038/181834a0
[19] J. Emsley, Nature's Building Blocks: Everything You Need to Know about the Elements, Oxford University Press, 2011.
[20] D.R. Lide, CRC Handbook of Chemistry and Physics, eighty fifth ed., CRC Press, Boca Raton, 2005, https://doi.org/10.1021/ja041017a
[21] M.J. Kirkham, A.M. Dos Santos, C.J. Rawn, E. Lara-Curzio, J.W. Sharp, A.J. Thompson, Abinitio determination of crystal structures of the thermoelectric material MgAgSb, Phys. Rev. B - Condens. Matter Mater. Phys. 85 (2012) 1–7, https://doi.org/10.1103/PhysRevB.85.144120
[22] H. Zhao, J. Sui, Z. Tang, Y. Lan, Q. Jie, D. Kraemer, K. McEnaney, A. Guloy, G. Chen, Z. Ren, High thermoelectric performance of MgAgSb-based materials, Nano Energy 7 (2014) 97–103, https://doi.org/10.1016/j.nanoen.2014.04.012
[23] Z. Liu, J. Mao, J. Sui, Z. Ren, High thermoelectric performance of α-MgAgSb for power generation, Energy Environ. Sci. 11 (2018) 23–44, https://doi.org/10.1039/c7ee02504a
[24] P. Ying, X. Liu, C. Fu, X. Yue, H. Xie, X. Zhao, W. Zhang, T. Zhu, High performance α-MgAgSb thermoelectric materials for low temperature power generation, Chem. Mater. 27 (2015) 909–913, https://doi.org/10.1021/cm5041826

[25] J. Sui, J. Shuai, Y. Lan, Y. Liu, R. He, D. Wang, Q. Jie, Z. Ren, Effect of Cu concentration on thermoelectric properties of nanostructured p-type $MgAg_{0.97-x}Cu_xSb_{0.99}$, Acta Mater. 87 (2015) 266–272, https://doi.org/10.1016/j.actamat.2015.01.018

[26] J. Shuai, H.S. Kim, Y. Lan, S. Chen, Y. Liu, H. Zhao, J. Sui, Z. Ren, Study on thermoelectric performance by Na doping in nanostructured $Mg_{1-x}Na_xAg_{0.97}Sb_{0.99}$, Nano Energy 11 (2015) 640–646, https://doi.org/10.1016/j.nanoen.2014.11.027

[27] Z. Liu, Y. Zhang, J. Mao, W. Gao, Y. Wang, J. Shuai, W. Cai, J. Sui, Z. Ren, The microscopic origin of low thermal conductivity for enhanced thermoelectric performance of Yb doped MgAgSb, Acta Mater. 128 (2017) 227–234, https://doi.org/10.1016/j.actamat.2017.02.015

[28] Y. Zheng, C. Liu, L. Miao, C. Li, R. Huang, J. Gao, X. Wang, J. Chen, Y. Zhou, E. Nishibori, Extraordinary thermoelectric performance in MgAgSb alloy with ultralow thermal conductivity, Nano Energy 59 (2019) 311–320, https://doi.org/10.1016/j.nanoen.2019.02.045

[29] Y. Zheng, C. Liu, L. Miao, H. Lin, J. Gao, X. Wang, J. Chen, S. Wu, X. Li, H. Cai, Cost effective synthesis of p-type Zn-doped MgAgSb by planetary ball-milling with enhanced thermoelectric properties, RSC Adv. 8 (2018) 35353–35359, https://doi.org/10.1039/C8RA06765A

[30] Z. Ren, Y. Lan, Q. Zhang, Advanced Thermoelectrics Materials, Contacts, Devices, and Systems, first ed., CRC Press, 2017, https://doi.org/10.1201/9781315153766-3

[31] J.L. Mi, P.J. Ying, M. Sist, H. Reardon, P. Zhang, T.J. Zhu, X.B. Zhao, B.B. Iversen, Elaborating the crystal structures of MgAgSb thermoelectric compound: polymorphs and atomic disorders, Chem. Mater. 29 (2017) 6378–6388, https://doi.org/10.1021/acs.chemmater.7b01768

[32] Z. Liu, J. Shuai, J. Mao, Y. Wang, Z. Wang, W. Cai, J. Sui, Z. Ren, Effects of antimony content in $MgAg_{0.97}Sb_x$ on output power and energy conversion efficiency, Acta Mater. 102 (2016) 17–23, https://doi.org/10.1016/j.actamat.2015.09.033

[33] Z. Liu, Y.Y. Wang, J. Mao, H. Geng, J. Shuai, Y.Y. Wang, R. He, W. Cai, J. Sui, Z. Ren, Lithium doping to enhance thermoelectric performance of MgAgSb with weak electron-phonon coupling, Adv. Energy Mater. 6 (2016) 1502269, https://doi.org/10.1002/aenm.201502269

[34] J. Lei, D. Zhang, W. Guan, Z. Ma, Z. Cheng, C. Wang, Y. Wang, Enhancement of thermoelectric figure of merit by the insertion of multi-walled carbon nanotubes in α-MgAgSb, Appl. Phys. Lett. 113 (2018), https://doi.org/10.1063/1.5042265

[35] Z. Liu, H. Geng, J. Mao, J. Shuai, R. He, C. Wang, W. Cai, J. Sui, Z. Ren, Understanding and manipulating the intrinsic point defect in α-MgAgSb for higher thermoelectric performance, J. Mater. Chem. A 4 (2016) 16834–16840, https://doi.org/10.1039/c6ta06832d

[36] D. Li, H. Zhao, S. Li, B. Wei, J. Shuai, C. Shi, X. Xi, P. Sun, S. Meng, L. Gu, Z. Ren, X. Chen, Atomic disorders induced by silver and magnesium ion migrations favor high thermoelectric performance in α-MgAgSb-based materials, Adv. Funct. Mater. 25 (2015) 6478–6488, https://doi.org/10.1002/adfm.201503022

[37] J. Lei, D. Zhang, W. Guan, Z. Cheng, C. Wang, Y. Wang, Engineering electrical transport in α-MgAgSb to realize high performances near room temperature, Phys. Chem. Chem. Phys. 20 (2018) 16729–16735, https://doi.org/10.1039/c8cp02186d

[38] T. Luo, F. Serrano-Sánchez, H. Bishara, S. Zhang, R. Bueno Villoro, J.J. Kuo, C. Felser, C. Scheu, G.J. Snyder, J.P. Best, G. Dehm, Y. Yu, D. Raabe, C. Fu, B. Gault, Dopant-segregation to grain boundaries controls electrical conductivity of n-type NbCo(Pt)Sn half-Heusler alloy mediating thermoelectric performance, Acta Mater. 217 (2021) 117147, https://doi.org/10.1016/j.actamat.2021.117147

[39] B.R.T. Frost, G.V. Raynor, The system silver-magnesium-antimony, with reference to the theory of alloy formation, Proc. R. Soc. Lond. Ser. A Math. Phys. Sci. 203 (1950) 132–147, https://doi.org/10.1098/rspa.1950.0130

[40] J.A. Kittl, K. Opsomer, C. Torregiani, C. Demeurisse, S. Mertens, D.P. Brunco, M.J.H. Van Dal, A. Lauwers, Silicides and germanides for nano-CMOS applications, Mater. Sci. Eng. B Solid State Mater. Adv. Technol. 154–155 (2008) 144–154, https://doi.org/10.1016/j.mseb.2008.09.033

[41] N. Oueldna, A. Portavoce, M. Bertoglio, M. Descoins, A. Kammouni, K. Hoummada, Seebeck coefficient in multiphase thin films, Mater. Lett. 266 (2020) 127460, https://doi.org/10.1016/j.matlet.2020.127460

[42] A. Portavoce, H. Khelidj, N. Oueldna, S. Amhil, M. Bertoglio, D. Mangelinck, L. Essaleh, K. Hoummada, Thermoelectric power factor of $Ge_{1-x}Sn_x$ thin films, Materialia 14 (2020) 100873, https://doi.org/10.1016/j.mtla.2020.100873

[43] C. Gayner, Y. Amouyal, Energy filtering of charge carriers: current trends, challenges, and prospects for thermoelectric materials, Adv. Funct. Mater. 30 (2020) 1901789, https://doi.org/10.1002/adfm.201901789

[44] N. Neophytou, S. Foster, V. Vargiamidis, G. Pennelli, D. Narducci, Nanostructured potential well/barrier engineering for realizing unprecedentedly large thermoelectric power factors, Mater. Today Phys. 11 (2019), https://doi.org/10.1016/j.mtphys.2019.100159

[45] D. Narducci, S. Frabboni, X. Zianni, Silicon de novo: energy filtering and enhanced thermoelectric performances of nanocrystalline silicon and silicon alloys, J. Mater. Chem. C 3 (2015) 12176–12185, https://doi.org/10.1039/c5tc01632k

[46] J.-F. Wang, X.-N. Fu, X.-D. Zhang, J.-T. Wang, X.-D. Li, Z.-Y. Jiang, Structural, elastic, electronic, and thermodynamic properties of MgAgSb investigated by density functional theory, Chin. Phys. B 25 (2016) 086302, https://doi.org/10.1088/1674-1056/25/8/086302

[47] A. Portavoce, E. Assaf, C. Alvarez, M. Bertoglio, R. Clérac, K. Hoummada, C. Alfonso, A. Charaï, O. Pilone, K. Hahn, V. Dolocan, S. Bertaina, Ferromagnetic MnCoGe thin films produced via magnetron sputtering and non-diffusive reaction, Appl. Surf. Sci. 437 (2018) 336–346, https://doi.org/10.1016/j.apsusc.2017.12.151